Nanoscale

PAPER

View Article Online
View Journal | View Issue

Cite this: *Nanoscale*, 2014, **6**, 8796

A facile green antisolvent approach to Cu^{2+}-doped ZnO nanocrystals with visible-light-responsive photoactivities†

Yi-Hsuan Lu,‡[a] Wei-Hao Lin,‡[a] Chao-Yao Yang,[a] Yi-Hsuan Chiu,[a] Ying-Chih Pu,[a] Min-Han Lee,[b] Yuan-Chieh Tseng[a] and Yung-Jung Hsu*[a]

An environmentally benign antisolvent method has been developed to prepare Cu^{2+}-doped ZnO nanocrystals with controllable dopant concentrations. A room temperature ionic liquid, known as a deep eutectic solvent (DES), was used as the solvent to dissolve ZnO powders. Upon the introduction of the ZnO-containing DES into a bad solvent which shows no solvation to ZnO, ZnO was precipitated and grown due to the dramatic decrease of solubility. By adding Cu^{2+} ions to the bad solvent, the growth of ZnO from the antisolvent process was accompanied by Cu^{2+} introduction, resulting in the formation of Cu^{2+}-doped ZnO nanocrystals. The as-prepared Cu^{2+}-doped ZnO showed an additional absorption band in the visible range (400–800 nm), which conduced to an improvement in the overall photon harvesting efficiency. Time-resolved photoluminescence spectra, together with the photovoltage information, suggested that the doped Cu^{2+} may otherwise trap photoexcited electrons during the charge transfer process, inevitably depressing the photoconversion efficiency. The photoactivity of Cu^{2+}-doped ZnO nanocrystals for photoelectrochemical water oxidation was effectively enhanced in the visible region, which achieved the highest at 2.0 at% of Cu^{2+}. A further increase in the Cu^{2+} concentration however led to a decrease in the photocatalytic performance, which was ascribed to the significant carrier trapping caused by the increased states given by excessive Cu^{2+}. The photocurrent action spectra illustrated that the enhanced photoactivity of the Cu^{2+}-doped ZnO nanocrystals was mainly due to the improved visible photon harvesting achieved by Cu^{2+} doping. These results may facilitate the use of transition metal ion-doped ZnO in other photoconversion applications, such as ZnO based dye-sensitized solar cells and magnetism-assisted photocatalytic systems.

Received 24th March 2014
Accepted 21st May 2014

DOI: 10.1039/c4nr01607f

www.rsc.org/nanoscale

Introduction

In the past few years, zinc oxide (ZnO) nanocrystals have driven countless studies due to their extensive applications ranging from photoelectronic physics to material chemistry.[1] Photoconversion using ZnO is of particular interest because it can practically harvest solar light to produce energy of other accessible forms.[2] Furthermore, ZnO is transparent and can be used as the conductive window layer in solar cells to improve the cell performance.[3] Despite the relatively non-toxic nature and high chemical stability, ZnO shows innately limited photoconversion performance under solar irradiation as a result of its large band gap which only allows light absorption in the UV region. Considerable research efforts have thus been undertaken to modulate the band structure of ZnO in order to make it responsive to visible light.[4] One effective approach to achieve this goal is to introduce foreign elements into ZnO, through which extra electronic states can be created within the energy gap of ZnO.[5] These dopant-induced electronic states may provide additional pathways for electronic transition, which results in the redshift of the absorption band towards the visible region. To date, various types of extrinsic dopants including metal cations[6] and non-metal anions[7] have been proven effective in promoting the visible light absorption of ZnO as well as enhancing the resultant photoconversion efficiency.

Recent developments have demonstrated the extensive use of doped ZnO nanocrystals in practical photoconversion applications. For example, Yang *et al.* designed N-doped ZnO nanowire arrays for application in photoelectrochemical water splitting.[8] Compared with pure ZnO, the N-doped ZnO electrode showed an order of magnitude increase in photocurrent generation with an enhanced photoactivity in the visible range, demonstrating the merits afforded by N dopants. N-doped ZnO

[a]*Department of Materials Science and Engineering, National Chiao Tung University, Hsinchu, Taiwan 30010, Republic of China. E-mail: yhsu@cc.nctu.edu.tw; Tel: +886 3 5712121 ext. 55317*

[b]*Undergraduate Honors Program of Nano Science and Engineering, National Chiao Tung University, Hsinchu, Taiwan 30010, Republic of China*

† Electronic supplementary information (ESI) available: TEM characterization, XPS spectra, UV-visible absorption spectra and magnetization curves of the samples. See DOI: 10.1039/c4nr01607f

‡ These authors contributed equally to this work.

has also been utilized as a highly efficient photocatalyst for promoting hydrogen production under visible light irradiation, as illustrated in Bhirud's study.[9] On the other hand, Cd^{2+}-doped ZnO particles were found to exhibit significantly enhanced photocatalytic performance in gaseous acetaldehyde degradation, which was attributed to the improved visible light harvesting.[10] The enhanced visible photocatalysis was also demonstrated in Co-doped ZnO, which showed one-fold increase in photocatalytic activity towards methylene blue degradation.[11] Among the various dopant ions, Cu^{2+} is regarded as one of the most promising candidates for achieving visible photoactivity for ZnO. By virtue of the small size mismatch as well as the similar electronic configuration with respect to Zn^{2+}, Cu^{2+} could be faultlessly introduced in the ZnO host with a concentration as high as 10 at%.[12] This attribute makes the more exact, quantitative study of the dopant effect for ZnO possible. A vast body of the literature has documented miscellaneous synthetic methods for the controlled growth of Cu^{2+}-doped ZnO nanocrystals. Most of them involve complicated preparation processes such as a prolonged reaction time,[13] an elevated reaction temperature,[1,14,15] post-annealing treatment,[16] or the use of environmentally harmful chemicals,[17] which may hinder the applicability of the products. Hence, the creation of a more effective, environmentally benign approach from which one can obtain Cu^{2+}-doped ZnO nanocrystals with controllable dopant concentrations is imperative more than ever before.

In this work, we developed an ultrafast, green, ionic liquid based antisolvent process for the preparation of Cu^{2+}-doped ZnO nanocrystals with well-defined morphology and controllable Cu^{2+} concentrations. It should be noted that all the chemicals used, including the precursors and solvents, were environmentally friendly, and the products were formed almost instantaneously at relatively low temperature. The antisolvent process involved the dissolution of ZnO powders in a deep eutectic solvent (DES), followed by the precipitation and growth of ZnO from the DES upon injection into a bad solvent. Here, "bad" is termed to describe the solvation behaviour of ZnO in a solvent where ZnO is hardly dissolved. Note that DESs are a new class of room temperature ionic liquids, which possess many fascinating solvent properties such as high polarity, high ionic conductivity, negligible vapour pressure and good thermal stability, being regarded as green solvents to replace the relatively hazardous organic solvents in many aspects.[18] The DES used here was prepared by mixing urea with choline chloride at a 2 : 1 molar ratio, which exhibits high solvency for many metal oxides, especially ZnO.[19] When ZnO-containing DES solution was injected into a bad solvent showing no solvation ability towards ZnO (*e.g.* water), ZnO was precipitated from the solution owing to the dramatic decrease in its solubility.[20] With the addition of Cu^{2+} to the bad solvent, growth of ZnO from the antisolvent process was accompanied by Cu^{2+} introduction, resulting in the formation of Cu^{2+}-doped ZnO nanocrystals. By modulating the amount of Cu^{2+} added, the concentration of Cu^{2+} doped in the ZnO nanocrystals can be readily controlled, from 1.0 to 10.0 at%. This feasibility enabled us to study the quantitative effect of Cu^{2+} doping on the photoconversion efficiency of ZnO. The as-prepared Cu^{2+}-doped ZnO nanocrystals showed effective light absorption in the visible range, attributable to the doped Cu^{2+} which invoked interband transitions within the energy gap of ZnO to enable a photoresponse to visible light. The doped Cu^{2+} may, however, trap photoexcited electrons during the charge transfer process to depress the resultant photoconversion efficiency. Photoelectrochemical measurements revealed that Cu^{2+}-doped ZnO nanocrystals with a Cu^{2+} concentration of 2.0 at% achieved the highest photocurrent of water oxidation, which is almost double the value of pure ZnO. A further increase in the Cu^{2+} concentration led to a consecutively depressed photocurrent generation, which was ascribed to the significant carrier trapping caused by the increased states given by excessive Cu^{2+}. The photocurrent action spectra manifested that the enhanced photoactivity of Cu^{2+}-doped ZnO nanocrystals was strongly correlated with the doped Cu^{2+} which promoted effective visible photon harvesting.

Experimental section

Chemicals

All the chemicals including urea (Riedel-de Haën, 99.5%), choline chloride (Sigma-Aldrich, 98%), ZnO powders (Sigma-Aldrich, 99%), ethylene glycol (Sigma-Aldrich, 99.8%) and copper nitrate (Sigma-Aldrich, 99%) were used without further purification.

Preparation of ZnO-containing DES

First, 150 g of DES, denoted as UCC, was prepared by mixing 69 g of urea and 81 g of choline chloride in a glovebox with an argon atmosphere. 0.36 g of ZnO powders was then added to the UCC to produce a solution containing roughly 2400 ppm of ZnO. The UCC solution was kept in an oven at 70 °C for several days until all the ZnO powders were dissolved.

Preparation of Cu^{2+}-doped ZnO nanocrystals

Ethylene glycol and deionized water mixed in an equal volume ratio were used as the bad solvent for ZnO. Copper nitrate of a desirable amount was then added to the bad solvent to provide a Cu^{2+} source for the doped samples. For the preparation of Cu^{2+}-doped ZnO nanocrystals, 5 mL of ZnO-containing DES was injected into 160 mL of the bad solvent in 5 s in a water bath maintained at 70 °C, followed by vigorous stirring for 30 min. With the presence of Cu^{2+} in the bad solvent, growth of ZnO from the antisolvent process was accompanied by Cu^{2+} doping. The resultant white suspending solid was collected by centrifugation at 8500 rpm for 5 min and washed with deionized water and ethanol to remove the remaining DES and impurities. The product was then dried at 60 °C in a vacuum for later use. In this work, various amounts of copper nitrate were employed to produce Cu^{2+}-doped ZnO nanocrystals with different Cu^{2+} concentrations (1.0, 2.0, 5.0 and 10.0 at%). For comparison purpose, pure ZnO nanocrystals were also prepared in the antisolvent process.

Photoelectrochemical measurement

The photoelectrochemical properties of the samples were examined in a three-electrode configuration cell with a Pt counter electrode, an Ag/AgCl reference electrode and a 0.5 M Na_2SO_4 electrolyte. The photoanode was prepared by dripping the sample suspension (20 μL, 0.2 mg mL^{-1}) on the fluorine-doped tin oxide (FTO) substrate (1.0 cm × 1.0 cm). The photoelectrochemical data were collected in an electrochemical station under white light illumination (500 W xenon lamp, 100 mW cm^{-2}). The photocurrent action spectra were measured under illumination of monochromatic light from the xenon lamp coupled with a monochromator.

Characterization

Field-emission scanning electron microscopy (SEM, JEOL, JSM-6500F) and high-resolution transmission electron microscopy (HRTEM, JEOL, JEM-2100) were used to examine the morphology and dimensions of the samples. Elemental analysis was conducted using energy dispersive X-ray spectrometry (EDS), an accessory of SEM and TEM. The crystallographic structure of the samples was characterized with selected-area electron diffraction (SAED, an accessory of TEM), and X-ray diffraction (XRD, Bruker, D2 phaser). Raman spectra were obtained using an excitation wavelength of 514.5 nm provided by an Ar laser with a power of 20 mW. During the measurement, a 100× objective with a numerical aperture of 0.9 was used. The absorption spectra were measured using a UV-visible spectrophotometer (Hitachi, U-3900H) equipped with a 5° specular reflectance attachment. For steady-state photoluminescence (PL) spectroscopy, a Kimmon IK3001R-G equipped with a He–Cd laser (720 W) was used. Time-resolved PL spectra were measured at room temperature using a single photon counting system (Horiba Jobin Yvon) that delivers an instrument response function down to 25 ps FWHM. A GaN diode laser (λ = 375 nm) was used as the excitation source. The signals collected at the emission of ZnO were dispersed with a grating spectrometer, detected by a high speed photomultiplier tube, and then correlated using a single photon counting card. The recorded emission decay data were analyzed and fitted with a biexponential kinetics model which generates two lifetime values, τ_1 and τ_2, and the corresponding amplitudes, A_1 and A_2. The intensity-average lifetime, $\langle\tau\rangle$, was determined using the following expression $\langle\tau\rangle = (A_1{\tau_1}^2 + A_2{\tau_2}^2)/(A_1\tau_1 + A_2\tau_2)$. All the fitting results are summarized in Table 1. Magnetization measurements of the samples were performed at room temperature using a vibrating sample magnetometer (VSM).

Table 1 Kinetic analysis of emission decay for the pure ZnO and Cu^{2+}-doped ZnO nanocrystals with different Cu^{2+} concentrations

	A_1 (%)	τ_1 (ns)	A_2 (%)	τ_2 (ns)	$\langle\tau\rangle$ (ns)
Pure ZnO	57.6	9.15	42.4	1.41	5.87
Cu^{2+}-doped ZnO, 1.0 at%	56.6	7.22	43.4	1.32	4.66
Cu^{2+}-doped ZnO, 2.0 at%	55.3	6.92	44.7	1.02	4.28
Cu^{2+}-doped ZnO, 5.0 at%	48.8	6.74	51.2	0.76	3.68
Cu^{2+}-doped ZnO, 10.0 at%	30.1	6.54	69.9	0.64	2.41

Results and discussion

The structures and dimensions of the samples were first investigated using SEM and TEM. Fig. 1 presents the SEM images of pure ZnO and the four doped samples with different Cu^{2+} concentrations. The pure ZnO nanocrystals were elliptically shaped and had a minor-axis length from 50 to 200 nm and a major-axis length up to 500 nm. HRTEM characterization (Fig. S1, ESI†) revealed that the pure ZnO was highly crystalline and structurally composed of two cones with round bottoms connected to each other. The major axis was found to be parallel to the [0001] direction, indicating a preferential growth direction of [0001] for the as-grown ZnO as consistent with previous results.[20] With the addition of Cu^{2+} ions to the bad solvent, growth of ZnO from the antisolvent process was accompanied by the introduction of Cu^{2+}. Upon increasing the amount of Cu^{2+}, the concentration of Cu^{2+} doped in ZnO nanocrystals increased accordingly. It is noteworthy that with the Cu^{2+} concentration increasing from 1.0 to 5.0 at%, the morphology of the doped ZnO remained elliptical, sharing a similar appearance to that of the pure ZnO. This morphological integrity is important to the exact interpretation of the dopant effect because the contribution from structural variation can be excluded. The sample with 10.0 at% Cu^{2+} was more rounded with reduced structural anisotropy along the *c*-axis. The detailed crystallographic structure of the Cu^{2+}-doped ZnO nanocrystals was analyzed by TEM and HRTEM. As displayed in Fig. 2, a preferential growth direction of [0001] was also observed for the Cu^{2+}-doped ZnO. This phenomenon suggested that the antisolvent growth of ZnO was rather independent of the introduction of Cu^{2+}. In Fig. 2(c), the HRTEM image taken on the doped ZnO clearly showed two distinct sets of lattice fringes that can be unambiguously assigned to the wurtzite ZnO. This finding is reasonable because the concentration of Cu^{2+} was essentially low and the radii of Zn^{2+} and Cu^{2+} are fairly close;[21] therefore no evident change in lattice orientation could be observed. The successful Cu^{2+} doping in ZnO nanocrystals can be confirmed by TEM-EDS analysis. As the inset of Fig. 2(c) shows, Cu^{2+} was uniformly distributed within the entire structure of ZnO, suggesting that homogeneous mixing of Cu^{2+} dopants with the host atoms of ZnO was achieved.

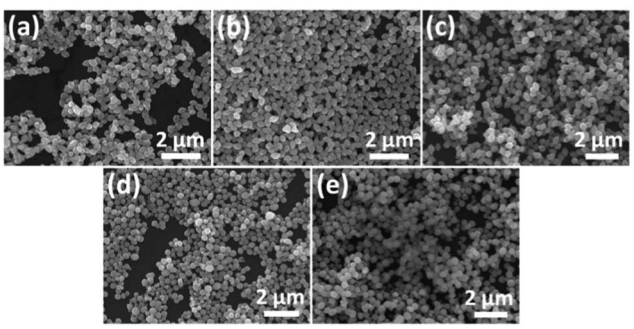

Fig. 1 SEM images of (a) the pure ZnO and Cu^{2+}-doped ZnO nanocrystals with Cu^{2+} concentrations of (b) 1.0 at%, (c) 2.0 at%, (d) 5.0 at% and (e) 10.0 at%.

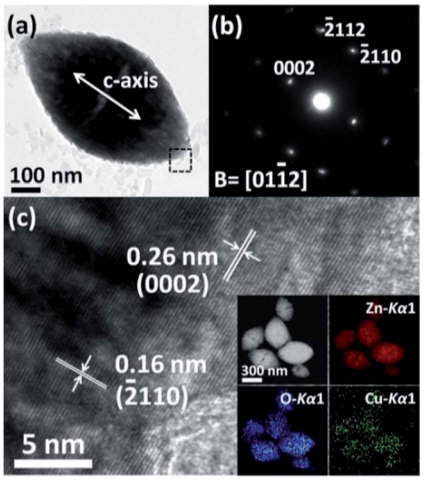

Fig. 2 (a) TEM image, (b) SAED pattern and (c) HRTEM image of Cu^{2+}-doped ZnO nanocrystals with 2.0 at% Cu^{2+}. The inset in (c) shows the TEM-EDS elemental mapping result.

To further elucidate the chemical nature of the dopant, XRD analysis and Raman study were conducted. Fig. 3(a) shows the XRD patterns of the pure ZnO and the four Cu^{2+}-doped ZnO samples. All the samples displayed clear diffraction peaks that can be assigned to the hexagonal wurtzite structure of ZnO (JCPDS 36-1451). The possibility of the secondary phases arising from Cu^{2+} doping is imperceptible in XRD, which is a support to the TEM-EDS analysis (Fig. 2(c)) from a macroscopic aspect. However, general broadening in all peaks and the shift towards a higher diffraction angle particular at (002) (inset of Fig. 2(a)) were noticeable in the sample with 10.0 at% Cu^{2+}. This means that the tolerance of the structural disordering for ZnO as well as its miscibility with Cu^{2+} may have reached the extremity at this concentration. Further doping is expected to cause significant modifications in the intrinsic crystallographic property that will likely mislead the cross-comparison among the samples.

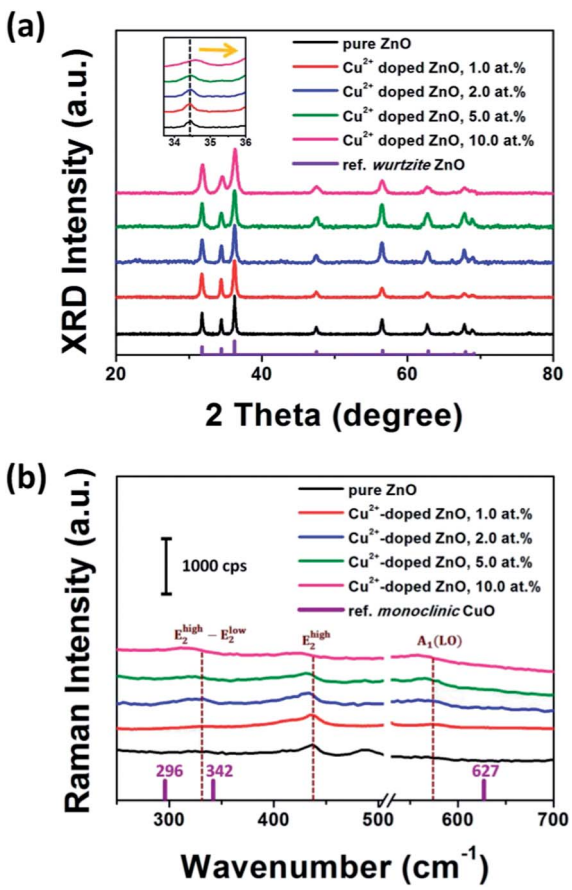

Fig. 3 (a) XRD patterns and (b) Raman spectra of the pure ZnO and Cu^{2+}-doped ZnO nanocrystals with different Cu^{2+} concentrations. The inset in (a) shows the enlarged part of the (002) peaks. The eliminated part in (b) is the signal from the Si substrate.

In addition to XRD, Raman spectroscopy also provides informative insights into the crystal structure and chemical composition of the sample,[22] which is particularly important to the doped ZnO because the possible secondary phase associated with the dopant can be further identified. ZnO crystals with the hexagonal wurtzite structure have C_{6v} symmetry,[23] which shows several vibrational modes including A_1(TO), A_1(LO), E_1(TO), E_1(LO), two B_1, and two E_2 modes. Among these modes, A_1, E_1, and E_2 are Raman active, while the two B_1 modes are silent modes that cannot be observed in Raman or IR spectra.[24] Due to back scattering geometry, some of the Raman active modes were not observed in our measurement.[25] As displayed in Fig. 3(b), the pure ZnO showed a dominant peak at 437 cm^{-1} which belongs to E_2^{high} mode. This mode is a representative characteristic of the hexagonal wurtzite structure resulting from the vibration of O sublattice.[26] A relatively weak peak at 574 cm^{-1} may represent the A_1(LO) mode, which is believed to be a defect-related mode.[25] In addition, the peak positioned at 331 cm^{-1} was regarded as the second-order scattering mode,[27] E_2^{high}–E_2^{low}. For all the doped samples, there were no signals related to the monoclinic CuO phase,[28] and all the Raman peaks recorded can be indexed to the vibrational modes from ZnO. Significantly, with the increase of the Cu^{2+} concentration, the prominent E_2^{high} mode was suppressed, red-shifted and broadened. This result was due to the decrease in the bonding energy of Zn–O and the lattice mismatch as a result of the substitution of Zn^{2+} by Cu^{2+}.[27] Similar results were reported in the literature that Cu-dopants may destroy the long-range order of the ZnO crystal to induce a pronounced change of the Raman feature.[27,29] On the other hand, the intensity of A_1(LO) was enhanced with increasing Cu^{2+} concentration, which was attributed to the generation of structural defects upon the Cu^{2+} introduction. The results of Raman spectra were consistent with those of XRD characterization, which confirmed that Cu^{2+} ions were substitutionally incorporated in ZnO nanocrystals without the formation of a secondary phase.

The optical properties of the samples were characterized with absorption and PL spectroscopy. Fig. 4 compares the UV-visible absorption spectra of the pure ZnO and Cu^{2+}-doped ZnO nanocrystals. The absorption edge in the UV region (about 375 nm) corresponded to the bandgap absorption of ZnO. Relative to pure ZnO, an additional absorption band in the visible range (400–700 nm) was observed for the four

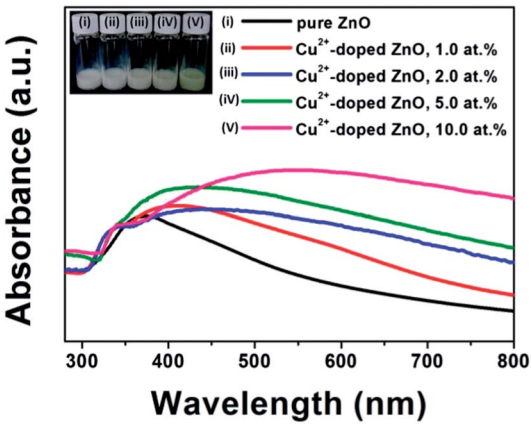

Fig. 4 UV-visible absorption spectra of the pure ZnO and Cu^{2+}-doped ZnO nanocrystals with different Cu^{2+} concentrations. The inset shows the corresponding suspension colours.

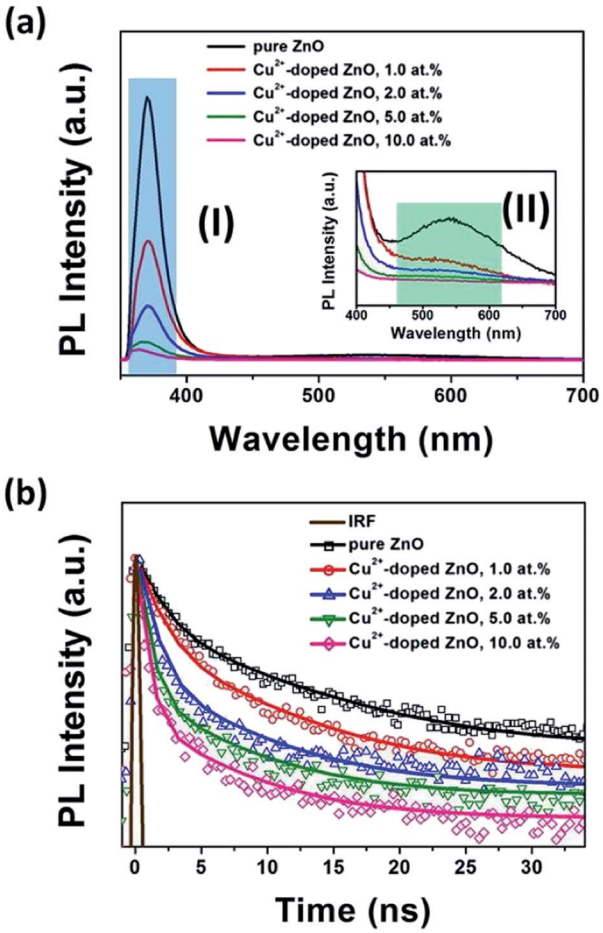

Fig. 5 (a) Steady-state PL spectra and (b) time-resolved PL spectra for the pure ZnO and Cu^{2+}-doped ZnO nanocrystals with different Cu^{2+} concentrations. The inset in (a) shows the enlarged part of the spectra at 400–700 nm. In (b), the instrumental response function (IRF) and the fitting results (solid curves) were also included for comparison.

Cu^{2+}-doped samples. It is generally accepted that the s–d or p–d exchange interactions between the dopants and host atoms may give rise to the dopant-induced states within the energy gap of ZnO.[30] These dopant-associated states provide additional pathways for electronic transition, thus resulting in the redshift of absorption towards the visible region. For the present Cu^{2+}-doped ZnO nanocrystals, the absorption in the visible region was attributed to the doped Cu^{2+} that invoked interband transitions. Because of this, ZnO can be excited by light with energy lower than the bandgap, generating extra charge carriers for further improving the photoconversion efficiency. In addition to the emergence of visible absorption, the colour change of ZnO upon Cu^{2+} doping was also evident. As illustrated in the inset of Fig. 4, the colour of Cu^{2+}-doped ZnO turned milky green with increasing Cu^{2+} concentration, similar to the phenomenon reported in a previous study.[31]

Fig. 5(a) shows the steady-state PL spectra of Cu^{2+}-doped ZnO nanocrystals compared with that of the pure ZnO. Two emission bands were observed in the wavelength range of 350 to 700 nm. The predominant UV emission at 385 nm (I) can be attributed to the excitonic band edge emission of ZnO.[32] The considerably minor green emission band at around 450–700 nm (II) was, however, ascribed to the trap-state emission of ZnO, which originated from the intrinsic defects such as oxygen vacancies.[32] After Cu^{2+} doping, the two emissions were greatly quenched. It has been suggested that the Cu^{2+} dopant may perform as an electron acceptor for ZnO,[33,34] which prohibited the recombination of photoinduced charge carriers. Because of the suppressed electron/hole recombination, the near band edge emission of ZnO was depressed for Cu^{2+}-doped ZnO. This proposition can be supported by the increasingly significant emission quenching observed for the samples with increasing Cu^{2+} concentrations. On the other hand, the declined green emission upon Cu^{2+} doping was assigned to the reduced amount of intrinsic defects of ZnO induced by the Cu^{2+} introduction.[35] The removal of intrinsic defects may assist in improving the photoconversion performance of ZnO by facilitating the charge carrier transfer. To further explore the Cu^{2+} doping effect on the charge carrier transfer of ZnO, time-resolved PL measurements were conducted. Fig. 5(b) compares the time-resolved PL spectra of the pure ZnO and the four Cu^{2+}-doped ZnO samples. Evidently, the doped ZnO exhibited a distinct PL decay behaviour from the pure ZnO, indicating the significant electronic interaction between the Cu^{2+} dopants and ZnO. The spectra in Fig. 5(b) were further fitted with a biexponential function which generates a slow (τ_1) and a fast (τ_2) decay component, assigned to radiative and nonradiative deactivation processes, respectively.[36,37] As noted in Table 1, both of the two decay components of ZnO were shortened by doping, suggesting that the Cu^{2+} dopants competed with the excited state deactivation in trapping the photoexcited electrons from the conduction band of ZnO. This result further illustrated that the Cu^{2+}-induced dopant states provided extra nonradiative pathways for charge carrier transfer, which was accountable for the shortening of the emission lifetime as well as the quenching of steady-state PL emission. Such Cu^{2+}-mediated carrier trapping became increasingly significant with increasing Cu^{2+} concentration, as evident from the gradually decreased lifetime observed for the sample. By comparing the average lifetime of

the pure ZnO and Cu^{2+}-doped ZnO,[38] we estimated that for the sample with 10.0 at% Cu^{2+}, approximately 54.6% of the electrons generated in ZnO following photoexcitation were transported and trapped at Cu^{2+} dopant levels.

For the present Cu^{2+}-doped ZnO nanocrystals, the effective light absorption in the visible range may conduce to the enhanced photoconversion performance. However, the moderate extent of carrier trapping mediated by the Cu^{2+} dopants could deteriorate the overall photoconversion efficiency by counteracting the merit of visible light harvesting. To investigate the effect of Cu^{2+} doping in the practical photoconversion process, photoelectrochemical measurements were performed by employing the samples as photoanodes for water oxidation. Fig. 6(a) depicts the chronoamperometric *I–t* curves of the pure ZnO and the four Cu^{2+}-doped ZnO nanocrystals recorded in the 0.5 M Na_2SO_4 electrolyte under chopped light illumination. All the electrodes showed a prompt response in photocurrent generation, indicating effective carrier transfer for the samples during the water oxidation process. With the introduction of 1.0 at% Cu^{2+}, the ZnO nanocrystal electrode showed a remarkably increased photocurrent density, confirming the positive role of Cu^{2+} dopants in enhancing the photoactivity of ZnO. Among all the doped samples tested, the one with 2.0 at% Cu^{2+} achieved the highest photocurrent generation, which is almost double the photocurrent density of the pure ZnO obtained at the same irradiation duration. When the Cu^{2+} concentration was more than 2.0 at%, the photocurrent density of the Cu^{2+}-doped ZnO electrode decreased significantly with an increase in the Cu^{2+} concentration. For the doped sample with 10.0 at% Cu^{2+}, the recorded photocurrent density even declined to one-tenth of the value of the pure ZnO. This photocurrent variation could be realized by the competition between visible light harvesting and charge carrier trapping at different Cu^{2+} concentrations. Under an essentially low Cu^{2+} concentration (*e.g.* 1.0 and 2.0 at%), effective visible light harvesting was vital for ZnO, thus generating extra charge carriers for promoting the photocatalysis. In the situation of relatively high Cu^{2+} concentration (*i.e.* 5.0 and 10.0 at%), carrier trapping mediated by Cu^{2+} was rather prevalent, giving rise to a counteraction effect to deplete the photoinduced charge carriers and thus the suppression in water splitting performance. It should be noted that the gradual decrease of photocurrent density during the on/off cycles of light illumination was related to the sample detachment from the FTO surface rather than the spoiling of the sample property associated with photocorrosion. As illustrated in Fig. S2 (ESI),† no appreciable change in the chemical composition was observed for the sample after being repeatedly used in photoelectrochemical processes, revealing the considerably high stability for the present Cu^{2+}-doped ZnO nanocrystals. To better understand the carrier trapping effect of Cu^{2+} in the photoelectrochemical cell, photovoltage decay measurement was performed, which has been considered as an effective method to investigate the trap state of a photoanode.[39] The photovoltage–time (*V–t*) spectra for all the samples were represented in Fig. 6(b), in which several important features can be observed. First, the voltage of ZnO prior to light irradiation, which represents the apparent Fermi level of the sample, shifted towards a more positive value with increasing Cu^{2+} concentration. This result inferred that the Fermi level of ZnO decreased with increasing Cu^{2+} concentration, which could be reasoned as being due to the p-type nature of the Cu^{2+} dopants in ZnO.[33,34] Second, the extent of photovoltage rise upon light irradiation was decreased for ZnO with increasing Cu^{2+} concentrations. Note that such a photovoltage rise derived from the accumulation of photoexcited electrons on the conduction band of ZnO,[40] which appeared less pronounced upon the introduction of Cu^{2+} because Cu^{2+} dopant states trapped photoexcited electrons from ZnO. Upon increasing the Cu^{2+} concentration, increasingly more photoexcited electrons on the conduction band of ZnO were rapidly transported to Cu^{2+} dopant states, prohibiting electron accumulation on the conduction band and thus reducing the photovoltage rise. Third, the photovoltage decay upon the cease of irradiation was deferred as the Cu^{2+} concentration was increased. To quantitatively compare the photovoltage decay, each *V–t* profile in Fig. 6(b) was fitted by a biexponential function with two time constants τ_1 and τ_2. The total half life, which equals to $\log(2\tau_1\tau_2/(\tau_1 + \tau_2))$, was calculated for comparison. The total half lives of the pure ZnO and Cu^{2+}-doped ZnO with 1.0, 2.0, 5.0 and 10.0 at% Cu^{2+} were estimated to be 1.80, 1.91, 1.96, 1.99 and

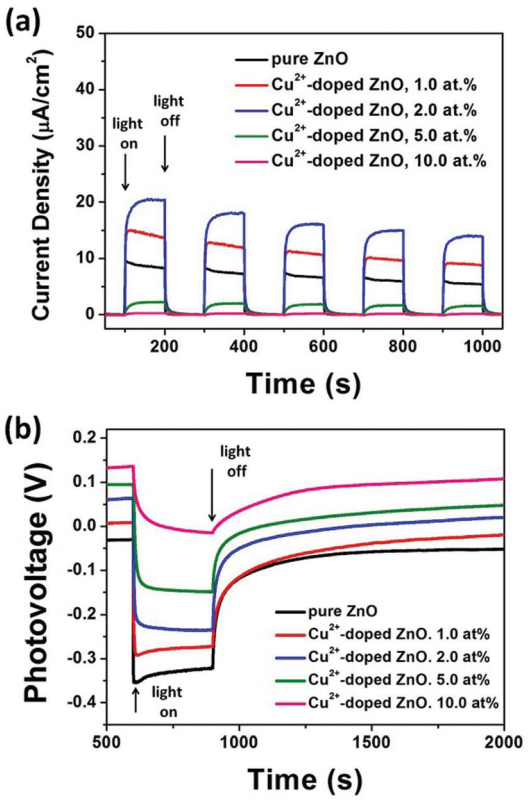

Fig. 6 (a) Chronoamperometric *I–t* curves collected at 0 V *vs.* Ag/AgCl for the pure ZnO and Cu^{2+}-doped ZnO nanocrystals with different Cu^{2+} concentrations under white light illumination. (b) Photovoltage–time spectra collected for the pure ZnO and Cu^{2+}-doped ZnO nanocrystals with different Cu^{2+} concentrations under white light illumination.

2.02 s, respectively. The evident increase of the total half life for ZnO with increasing Cu^{2+} concentrations can be attributed to the fact that the Cu^{2+}-mediated carrier trapping was increasingly significant. Once the photoexcited electrons were trapped at Cu^{2+} dopant states, their release to the valence band became difficult, making the photovoltage decay more sustainable than that of the pure ZnO. The photovoltage measurements further validated the carrier trapping nature of the Cu^{2+} dopants for the present Cu^{2+}-doped ZnO nanocrystals in the photoelectrochemical cell, which matched well with the observation of time-resolved PL analysis.

To further explore the photoactive wavelength regime for the Cu^{2+}-doped ZnO nanocrystals, the photocurrent values at different illumination wavelengths were measured. Fig. 7 presents the photocurrent action spectra of three representative samples. For the pure ZnO nanocrystals, a minimal photoresponse was noticed beyond 400 nm, which is expectable since this region was below the bandgap energy of ZnO. For the sample with 2.0 at% Cu^{2+}, remarkably enhanced photoactivity across the entire UV-visible region was recorded. The photocurrent increase in the UV region was mainly due to the reduced amount of intrinsic defects as evidenced by the green emission quenching observed in Fig. 5(a). The photocurrent enhancement in the visible range could be direct evidence that the Cu^{2+} dopants promoted effective visible light harvesting for ZnO to improve the photoconversion efficiency. As for the sample with 5.0 at% Cu^{2+}, the photocurrent density was depressed in the entire UV-visible region. The significant carrier trapping caused by the increased amount of Cu^{2+} dopant states could be responsible for this outcome. It is worth mentioning that the photoactivity of the sample with 5.0 at% Cu^{2+} was still notable in the visible region although the overall photocurrent generation was quite mediocre. This observation illustrated that the present Cu^{2+}-doped ZnO nanocrystals were visible light responsive even when the Cu^{2+} concentration was so high that Cu^{2+}-mediated carrier trapping became virtually detrimental to the photoconversion performance.

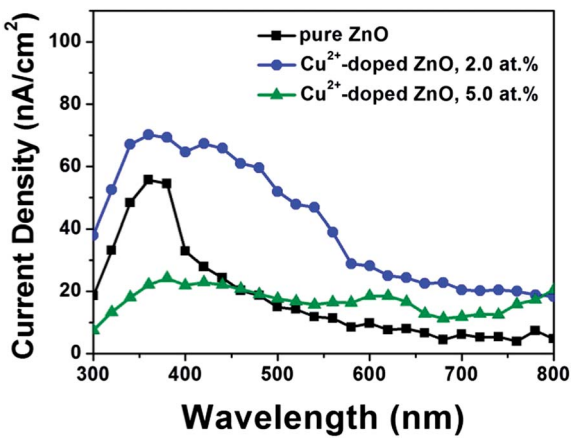

Fig. 7 Photocurrent action spectra for the pure ZnO and the two Cu^{2+}-doped ZnO nanocrystals collected at 0 V *vs.* Ag/AgCl in the wavelength range from 300 to 800 nm.

Conclusions

In conclusion, we have successfully prepared Cu^{2+}-doped ZnO nanocrystals using a facile, green antisolvent approach. Unlike other synthetic systems which use relatively complicated procedures, the current antisolvent approach provided considerable feasibility of obtaining doped ZnO nanocrystals with controllable dopant concentrations. Further extension to obtain other metal ion-doped ZnO is possible, for example, Ni^{2+}-doped ZnO nanocrystals as demonstrated in Fig. S3 (ESI).† As a result of the improved visible light harvesting, Cu^{2+}-doped ZnO nanocrystals exhibited remarkably enhanced photoactivity in the photoelectrochemical water splitting. However, significant carrier trapping caused by the excess Cu^{2+} gave rise to a counteraction effect to deplete the photoinduced charge carriers, thus resulting in the depressed water oxidation performance. On the other hand, due to the sp–d exchange interaction, the as-prepared Cu^{2+}-doped ZnO nanocrystals exhibited room temperature ferromagnetism where the saturation magnetization increased with increasing Cu^{2+} concentration (Fig. S4, ESI†). The visible light responsiveness as well as the room temperature ferromagnetism makes the present Cu^{2+}-doped ZnO nanocrystals especially promising in unique magneto-optical applications, in which the photoconversion performance may be dictated by both visible light excitation and external field exertion.[41,42]

Acknowledgements

This work was supported by the Ministry of Science and Technology of the Republic of China (Taiwan) under grant NSC-102-2113-M-009-005-MY2.

Notes and references

1 (*a*) Z. W. Pan, Z. R. Dai and Z. L. Wang, *Science*, 2001, **291**, 1947; (*b*) P. Sharma, A. Gupta, K. V. Rao, F. J. Owens, R. Sharma, R. Ahuja, J. M. O. Guillen, B. Johansson and G. A. Gehring, *Nat. Mater.*, 2003, **2**, 673; (*c*) R. L. Hoffman, *J. Appl. Phys.*, 2004, **95**, 5813.

2 (*a*) K.-S. Ahn, Y. Yan, S. Shet, K. Jones, T. Deutsch, J. Turner and M. Al-Jassim, *Appl. Phys. Lett.*, 2008, **93**, 163117; (*b*) A. Mclaren, T. Valdes-Solis, G. Li and S. C. Tsang, *J. Am. Chem. Soc.*, 2009, **131**, 12540; (*c*) X. Lu, G. Wang, S. Xie, J. Shi, W. Li, Y. Tong and Y. Li, *Chem. Commun.*, 2012, **48**, 7717.

3 (*a*) K. P. Musselman, A. Wisnet, D. C. Iza, H. C. Hesse, C. Scheu, J. L. MacManus-Driscoll and L. Schmidt-Mende, *Adv. Mater.*, 2010, **22**, E254; (*b*) Y. Liu, H. K. Turley, J. R. Tumbleston, E. T. Samulski and R. Lopez, *Appl. Phys. Lett.*, 2011, **98**, 162105; (*c*) M. Thambidurai, J. Y. Kim, C. Kang, N. Muthukumarasamy, H.-J. Song, J. Song, Y. Ko, D. Velauthapillai and C. Lee, *Renewable Energy*, 2014, **66**, 433.

4 P. V. Radovanovic and D. R. Gamelin, *Phys. Rev. Lett.*, 2003, **91**, 157202.

5 L. J. Zhang, J. Q. Wang, J. Li, J. Zhou, W. P. Cai, J. Cheng, W. Xu, G. Yin, X. Wu, Z. Jiang, S. Zhang and Z. Y. Wu, *Chem. Commun.*, 2012, **48**, 91.
6 S. Liu, C. Li, J. Yu and Q. Xiang, *CrystEngComm*, 2011, **13**, 2533.
7 T. C. Kaspar, T. Droubay, S. M. Heald, M. H. Engelhard, P. Nachimuthu and S. A. Chambers, *Phys. Rev. B: Condens. Matter Mater. Phys.*, 2008, **77**, 201303.
8 X. Yang, F. Qian, J. Z. Zhang and Y. Li, *Nano Lett.*, 2009, **9**, 2331.
9 A. P. Bhirud, S. D. Sathaye, R. P. Waichal, L. K. Nikama and B. B. Kale, *Green Chem.*, 2012, **14**, 2790.
10 S. Anandana, N. Ohashib and M. Miyauchia, *Appl. Catal., B*, 2010, **100**, 502.
11 B. M. Rajbongshi and S. K. Samdarshi, *Appl. Catal., B*, 2014, **144**, 435.
12 M. Pashchanka, R. C. Hoffmann, A. Gurlo, J. C. Swarbrick, J. Khanderi, J. Engstler, A. Issanin and J. J. Schneider, *Dalton Trans.*, 2011, **40**, 4307.
13 H. Zhang, D. Yang, D. Li, X. Ma, S. Li and D. Que, *Cryst. Growth Des.*, 2005, **5**, 547.
14 W. I. Park, G. Yi, M. Kim and S. L. Pennycook, *Adv. Mater.*, 2002, **14**, 1841.
15 M. H. Huang, Y. Wu, H. Feick, N. Tran, E. Weber and P. Yang, *Adv. Mater.*, 2001, **13**, 113.
16 B. Liu and H. C. Zeng, *J. Am. Chem. Soc.*, 2003, **125**, 4430.
17 J. Joo, S. G. Kwan, J. H. Yu and T. Hyeon, *Adv. Mater.*, 2005, **17**, 1873.
18 K. R. Seddon, *J. Chem. Technol. Biotechnol.*, 1997, **68**, 351.
19 A. P. Abbott, G. Capper, D. L. Davies, R. K. Rasheed and P. Shikotra, *Inorg. Chem.*, 2005, **44**, 6497.
20 J. Y. Dong, Y. J. Hsu, D. S. H. Wong and S. Y. Lu, *J. Phys. Chem. C*, 2010, **114**, 8867.
21 R. D. Shannon, *Acta Crystallogr.*, 1976, **A32**, 751.
22 K. Samanta, S. Dussan, R. S. Katiyar and P. Bhattacharya, *Appl. Phys. Lett.*, 2007, **90**, 261903.
23 X. B. Wang, C. Song, K. W. Geng, F. Zeng and F. Pan, *Appl. Surf. Sci.*, 2007, **253**, 6905.
24 R. Cusco, E. A. Llado, J. Ibanez, L. Artus, J. Jimenez, B. Wang and M. J. Callahan, *Phys. Rev. B: Condens. Matter Mater. Phys.*, 2007, **75**, 165202.
25 Z. Q. Chen, M. Maekawa, A. Kawasuso, S. Sakai and H. Naramoto, *J. Appl. Phys.*, 2006, **99**, 093507.
26 J. M. Calleja and M. Cardona, *Phys. Rev. B: Solid State*, 1977, **16**, 3753.
27 Y. Jin, Q. Cui, G. Wen, Q. Wang, J. Hao, S. Wang and J. Zhang, *J. Phys. D: Appl. Phys.*, 2009, **42**, 215007.
28 T. Yu, X. Zhao, Z. X. Shen, Y. H. Wu and W. H. Su, *J. Cryst. Growth*, 2004, **268**, 590.
29 J. Mohapatra, D. K. Mishra, V. Berma, S. K. Kamilla, R. Sakthivel, B. K. Mohapatra and S. K. Singh, *Adv. Sci. Lett.*, 2011, **4**, 458.
30 (*a*) Y. D. Kim, S. L. Cooper, M. V. Klein and B. T. Jonker, *Phys. Rev. B: Condens. Matter Mater. Phys.*, 1994, **49**, 1732; (*b*) Q. Xiao and J. Zhang, *Mater. Sci. Eng., B*, 2007, **142**, 121.
31 F. G. Gartner and E. Mollwo, *Phys. Status Solidi B*, 1978, **89**, 381.
32 R. B. Kale, Y. J. Hsu, Y. F. Lin and S. Y. Lu, *Solid State Commun.*, 2007, **142**, 302.
33 M. D. McCluskey and S. J. Jokela, *J. Appl. Phys.*, 2009, **106**, 071101.
34 R. Dingle, *Phys. Rev. Lett.*, 1969, **23**, 579.
35 R. Elilarassi and G. Chandrasekaran, *J. Mater. Sci.: Mater. Electron.*, 2010, **21**, 1168.
36 W. S. Chae, J. H. Ko, I. W. Hwang and Y. R. Kim, *Chem. Phys. Lett.*, 2002, **365**, 49.
37 S. Sadhu, P. S. Chowdhury and A. Patra, *J. Lumin.*, 2008, **128**, 1235.
38 C. Harris and P. V. Kamat, *ACS Nano*, 2010, **4**, 7321.
39 B. Mukherjee, W. Wilson and V. R. Subramanian, *Nanoscale*, 2013, **5**, 269.
40 J. Bisquert, A. Zaban, M. Greenshtein and I. M. Seró, *J. Am. Chem. Soc.*, 2004, **126**, 1355.
41 W. Zhang, X. Wang and X. Fu, *Chem. Commun.*, 2003, 2196.
42 Y. Cui, J. Briscoe and S. Dunn, *Chem. Mater.*, 2013, **25**, 4215.